Chemical Physics Letters 739 (2020) 136959

Contents lists available at ScienceDirect

Chemical Physics Letters

journal homepage: www.elsevier.com/locate/cplett

Research paper

Controllable interfacial adhesion behaviors of polymer-on-polymer surfaces during fused deposition modeling 3D printing process

Xu Zhang[a,*], Jianlei Wang[b,*]

[a] Innovation Center for Textile Science and Technology, Donghua University, Shanghai 201620, PR China
[b] CAS Key Laboratory of Design and Assembly of Functional Nanostructures, and Fujian Key Laboratory of Nanomaterials, Fujian Institute of Research on the Structure of Matter, Chinese Academy of Sciences, Fuzhou, Fujian 350002, PR China

HIGHLIGHTS

- The interfacial bonding strength of polymer-on-polymer surfaces can be availably tailored by the filling density and cooling rate.
- As the filling density increases, the interfacial bonding strength firstly increases to an optimal value and then decreases.
- The better strength of interfacial adhesion is mainly attributed to the larger width of wetted interface and degree of inter-molecular diffusion between two adjacent layers.

ARTICLE INFO

Keywords:
Interfacial adhesion
Inter-molecular diffusion
Mechanical property
Fused deposition modeling
3D printing
Self-consistent field theory

ABSTRACT

The controllable interfacial adhesion behaviors of polymer-on-polymer surfaces during fused deposition modeling (FDM) three-dimensional (3D) printing process were examined by combining the experimental tests and self-consistent field theory (SCFT) to further get insight into the interfacial bonding behaviors between currently- and previously-deposited layers. The results show that the interfacial bonding strength can be availably tailored by the filling density and cooling rate. An unusual and interesting phenomenon was also observed that the interfacial bonding strength firstly increases to an optimal value and then decreases as the filling density increases. Both the experimental observations and SCFT calculations revealed that the better strength of interfacial adhesion is mainly attributed to the larger width of wetted interface and degree of inter-molecular diffusion between two adjacent layers. The critical mechanism behind the controllable interfacial adhesion strength of polymer-on-polymer surfaces were precisely clarified. The present work may provide useful information for preparing lightweight FDM parts with high performance and a general understanding of the interfacial bonding behaviors of polymer-on-polymer surfaces.

1. Introduction

Additive manufacturing (AM), also so-called three-dimensional (3D) printing, has been leading to a mold-less era, which has captured a wide horizon [1,2] and is also developing at an incredible pace in the speed and accuracy of printing models with complex geometries and low manufacturing cost, representing a new edge on prototyping process evolution [3,4]. As the trendiest technique among all AM technologies, the fused deposition modeling (FDM) shows the high potential for fabricating 3D-printed parts with the capacity to compete with conventional processing techniques [5,6]. Moreover, the potential to grow mostly depends on the materials available for FDM process, so it is meaningful to develop new materials to further broaden the range of its applications [7–13]. Although, the FDM 3D printing is an effective tool to realize the optimal design with various materials, there still remain a critical problem of achieving an adequate level of mechanical strength for FDM products due to the discontinuous nature of the FDM process, where a molten filament is extruded and deposited onto the previously deposited layers to form interfacial bonds with adjacent filaments. The mechanical properties of the FDM 3D-printed parts are far weaker than that of the parts fabricated by traditional methods such as the injection moulding [14].

In addition to new materials, the processing parameter optimization is also a critical factor to improve the mechanical properties of FDM 3D-printed parts. Also, several studies focused on discovering the relationship between the mechanical properties of the FDM 3D-printed

* Corresponding authors.
E-mail addresses: xuzhang@dhu.edu.cn (X. Zhang), jlwang@fjirsm.ac.cn (J. Wang).

https://doi.org/10.1016/j.cplett.2019.136959
Received 25 October 2019; Received in revised form 9 November 2019; Accepted 12 November 2019
Available online 13 November 2019

parts and the processing parameters during FDM process, such as raster angle and gap [15–17], layer thickness [17,18], printing orientation [17–19], post-processing [10,20,21], and other external environmental conditions [22]. Despite of the advanced development of FDM 3D printing materials and technologies, the systematic research on the interfacial bonding behaviors between the extruding molten filaments and the previously deposited layers during the FDM process is seldom concerned. Also, the mechanism and impact factor behind the interfacial bonding strength of FDM 3D-printed parts is still unclear. Here, we demonstrated the effect of environmental cooling rate on the interfacial bonding strength of FDM 3D-printed parts by combining the mean-field theory to further get insight into the interfacial bonding behaviors between the previously-deposited and current layers.

2. Methods

2.1. Experimental section

In the present work, the poly(lactic acid) (PLA) masterbatches (3052D, NatureWorks, USA) were extruded in a single-crew extruder (SHSJ45, Songhu Co., China) to prepare the fused deposition modeling (FDM) 3D printing PLA filaments with 1.75 mm in diameter. During the process, the barrel temperature ranged between 190 °C and 240 °C. The tensile samples were prepared by feeding the PLA filaments into a commercial desktop FDM unit with two nozzles (MakerPI M2030X, Soongon Co. Ltd., Shenzhen, China), which could feed two different materials mixing with different feeding speed at the same time. Near the nozzle in the FMD 3D printing machine, there are two small air fans with identical rev on the opposite side to cool down the previously deposited layers. The rev of the two fans can be identically tailored from 100% to 0% corresponding to the cooling rate, where the higher rev of the two fans represents the faster cooling rate. The diameter of the nozzle in FDM unit is 0.5 mm, ensuring that no clogging happens during FDM 3D printing process.

The modified ISO 527 5A dog-bone dimensions with pipe cylinder dimensions (Scheme 1) were followed. The specimens were conducted in a universal testing machine (AGS-X Shimadzu Co., Kyoto, Japan) with a 100 kN transducer capacity. The cross-head speed for tensile tests were 2 mm/min. The SEM micrographs of the fracture surfaces were taken with Hitachi SU8010 FEG-SEM with an acceleration voltage of 5 kV after specimens were fractured in liquid nitrogen.

2.2. Self-consistent field theory

As shown in Scheme 2, we consider an incompressible system with

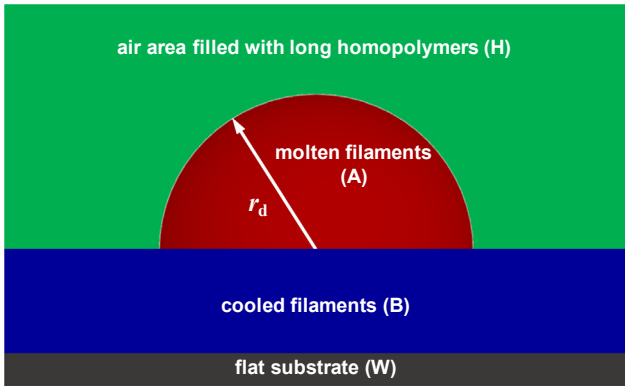

Scheme 2. Scheme of the currently-molten filaments (A) deposited on the previously-cooled filaments.

total volume V, containing n_A monodisperse homopolymers (A) soft-confined in a fluid droplet with a fixed volume V_A spreading on the surfaces of the n_B cooled monodisperse homopolymers (B) with the same length to A ($N_A = N_B = N$), n_H long homopolymers (H) to fill the air region surrounding the droplet, and n_w wall "particles" to construct the flat solid substrate (W). The polymer chains (A, B, and H) are treated as Gaussian chains with the same statistical segment length a and a fixed segment volume ρ_0^{-1}.

Within the SCFT framework, the configuration of a single polymer chain is determined by a set of effective chemical potential fields $\omega_I(\mathbf{r})$ to replace the actual interactions, where I denotes A-, B-, and H-species. The potential fields are conjugated to the density fields $\phi_I(\mathbf{r})$. We invoke an incompressibility ($\phi_A(\mathbf{r}) + \phi_B(\mathbf{r}) + \phi_H(\mathbf{r}) + \phi_W(\mathbf{r}) = 1$) by introducing a Lagrange multiplier $\xi(\mathbf{r})$ that enforces the incompressibility constraint. The free energy per chain is given by

$$\frac{NF}{\rho_0 k_B T V} = \frac{1}{V}\int d\mathbf{r} \sum_{\substack{I,J=A,B,H,W \\ I\neq J}} \frac{1}{2}\chi_{IJ} N \phi_I(\mathbf{r})\phi_J(\mathbf{r}) - \frac{1}{V}\int d\mathbf{r}\left\{\sum_{I=A,B,H}\omega_I(\mathbf{r})\phi_I(\mathbf{r}) + \xi(\mathbf{r})\left[1 - \sum_{I=A,B,H,W}\phi_I(\mathbf{r})\right]\right\} - c_A \ln\left(\frac{Q_A}{V}\right) - c_B \ln\left(\frac{Q_B}{V}\right) - \frac{c_H}{\alpha}\ln\left(\frac{Q_H}{V}\right) \quad (1)$$

where k_B is the Boltzmann constant; T is the temperature; χ_{IJ} is the Flory-Huggins parameter between I- and J- species; $c_A = V_A/V$, $c_B = V_B/V$, and $c_H = V_H/V$ is the volume fraction of A homopolymers (B homopolymers or long H homopolymers); α is the ratio of the long H

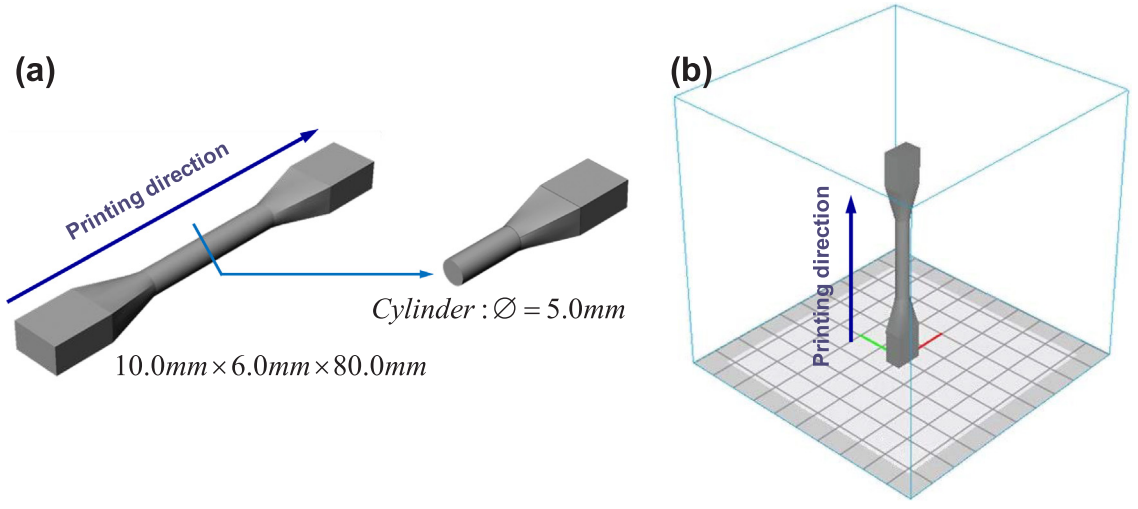

Scheme 1. (a) 3D Model of the specimen used for FDM 3D printing and (b) FDM 3D printing process.

homopolymer length N_H to A homopolymer length N, i.e. $\alpha = N_H/N$. Q_A, Q_B, and Q_H is the partition function of a single non-interacting A, B, and H polymer chain subject to the fields $\omega_A(\mathbf{r})$, $\omega_B(\mathbf{r})$, and $\omega_H(\mathbf{r})$ in terms of the backbone propagator $q_A(\mathbf{r},s)$, $q_B(\mathbf{r},s)$, and $q_H(\mathbf{r},s)$, respectively. The spatial coordinate $\mathbf{r}$ is rescaled by R_g, where $R_g{}^2 = a^2N/6$.

For the A and B homopolymers (I = A or B), the propagator satisfies the following modified diffusion equation

$$\frac{\partial q_I(\mathbf{r}, s)}{\partial s} = \nabla^2 q_I(\mathbf{r}, s) - \omega_I(\mathbf{r}) q_I(\mathbf{r}, s) \tag{2}$$

and is subject to the initial condition $q_I(\mathbf{r},0) = 1$ for the free end of the I (=A or B) homopolymer chain at $s = 0$. In terms of the propagator $q_I(\mathbf{r},s)$, the single chain partition function can be computed by

$$Q_I = \int d\mathbf{r} q_I(\mathbf{r}, 1) \tag{3}$$

In addition, the backward propagator $q_I{}^+(\mathbf{r},s)$ of each A hand B homopolymer chain is also defined, which satisfies the same diffusion equation to $q_I(\mathbf{r},s)$, Eq. (2), subject to the initial condition $q_I{}^+(\mathbf{r},0) = 1$, and starts on the other free end of the I (=A or B) homopolymer chain.

For the long H homopolymers filled the air region surrounding the droplet, the partition function $q_H(\mathbf{r},s)$ also stratifies the same diffusion equation subject to the long H homopolymer field $\omega_H(\mathbf{r})$, but now s runs from 0 to $\alpha = N_H/N$, and is given by

$$\frac{N}{N_H}\frac{\partial q_H(\mathbf{r}, s)}{\partial s} = \nabla^2 q_H(\mathbf{r}, s) - \omega_H(\mathbf{r}) q_H(\mathbf{r}, s) \tag{4}$$

subject to the initial condition $q_H(\mathbf{r},0) = 1$. To further calculate the homopolymer density $\phi_H(\mathbf{r})$, we approximate the $q_H(\mathbf{r},s)$ at $\alpha = 4$ which is accurate enough to reduce the relative error [23]. Besides, the single chain partition function can be further calculated by

$$Q_H = \int d\mathbf{r} q_H(\mathbf{r}, \alpha) \tag{5}$$

In accordance with the propagators and partition functions, the segment densities $\phi_A(\mathbf{r})$, $\phi_B(\mathbf{r})$, and $\phi_H(\mathbf{r})$ follow that

$$\phi_A(\mathbf{r}) = \frac{c_A V}{Q_A}\int_0^1 ds q_A(\mathbf{r}, s) q_A{}^+(\mathbf{r}, 1-s) \tag{6}$$

$$\phi_B(\mathbf{r}) = \frac{c_B V}{Q_B}\int_0^1 ds q_B(\mathbf{r}, s) q_B{}^+(\mathbf{r}, 1-s) \tag{7}$$

$$\phi_H(\mathbf{r}) = \frac{c_H V}{Q_H}\int_0^\alpha ds q_H(\mathbf{r}, s) q_H(\mathbf{r}, \alpha-s) \tag{8}$$

Finally, the minimization of free energy with respect to $\phi_A(\mathbf{r})$, $\phi_B(\mathbf{r})$, $\phi_H(\mathbf{r})$, and $\xi(\mathbf{r})$ is achieved by satisfying the mean-field equations

$$\omega_A(\mathbf{r}) = \chi_{AB}N\phi_B(\mathbf{r}) + \chi_{AH}N\phi_H(\mathbf{r}) + \chi_{AW}N\phi_W(\mathbf{r}) + \xi(\mathbf{r}) \tag{9}$$

$$\omega_B(\mathbf{r}) = \chi_{AB}N\phi_A(\mathbf{r}) + \chi_{BH}N\phi_H(\mathbf{r}) + \chi_{BW}N\phi_W(\mathbf{r}) + \xi(\mathbf{r}) \tag{10}$$

$$\omega_H(\mathbf{r}) = \chi_{AH}N\phi_A(\mathbf{r}) + \chi_{BH}N\phi_B(\mathbf{r}) + \chi_{HW}N\phi_W(\mathbf{r}) + \xi(\mathbf{r}) \tag{11}$$

$$\phi_A(\mathbf{r}) + \phi_B(\mathbf{r}) + \phi_H(\mathbf{r}) + \phi_W(\mathbf{r}) = 1 \tag{12}$$

The density field of wall "particles" $\phi_W(\mathbf{r})$ is a fixed function of $\mathbf{r}$ that is specified before starting the SCFT simulations, following the "masking" technique proposed by Fredrickson et al. [24] and extended by others [25–27]. The transition of $\phi_W(\mathbf{r})$ is selected to be a hyperbolic tangent form, which is as follows

$$\phi_W(\mathbf{r}) = \frac{1}{2}\left\{1 + \tanh\left[\lambda\frac{d(\mathbf{r})}{\sigma}\right]\right\} \tag{13}$$

where λ and σ are factors used to define the transition region and set the width of the transition region, respectively; $d(\mathbf{r})$ is the distance from the point $\mathbf{r}$ to the edge of the boundary of the wall. We assume that the boundary of the wall is at $\phi_W(\mathbf{r}) = 0.5$, and select $\lambda = \log(99) = 4.5951$ such that the wall transition region begins at $\phi_W(\mathbf{r}) = 0.01$ and ends at $\phi_W(\mathbf{r}) = 0.99$. The σ is set to be $0.5R_g$ which approximately equals to the interface width. Note that the σ value couldn't affect the results as suggested by Fredrickson et al. [24]. This "masking" technique can retain the stability characteristics of standard saddle point search methods and is particularly suited for the numerical implement of the SCFT equations by pseudo-spectral method.

The simulations in this work were carried out in the two-dimensions with periodic boundary conditions owing to the "masking" technique. The numerical solution of the mean-field equations was started from a random initial states by confining A homopolymers in a semi-sphere on the surfaces of cooled B homopolymers and filling the air region surrounding the droplet with long H homopolymers, see Scheme 2. The modified diffusion equations were solved *via* the pseudo-spectral method and operator splitting formula scheme. In the calculations, the spatial resolutions were taken as $\Delta x < 0.1R_g$ and the contour step sizes were set at $\Delta s = 0.01$. The numerical simulations proceeded until the relative accuracy in the fields is smaller than 10^{-6} and the incompressibility condition was achieved [28].

3. Results and discussion

3.1. Adhesion strength

In the present study, the effect of filling density (denoted by ρ_f) and cooling rate (measured by the rev of the cooling fan and denoted by υ) on the interfacial bonding strength (denoted by σ_b) of the FDM 3D-printed parts were significantly investigated. As shown in Fig. 1a, it can be seen that the interfacial bonding strength shows an increase as the cooling rate decreases at a certain fixed filling density. Take the filling density ρ_f = 90% as an example (the olive line in Fig. 1a), the interfacial bonding strength gradually increases from 30.8 MPa to 32.5 MPa to 33.9 MPa to 35.4 MPa to 36.4 MPa and then to 36.9 MPa as the

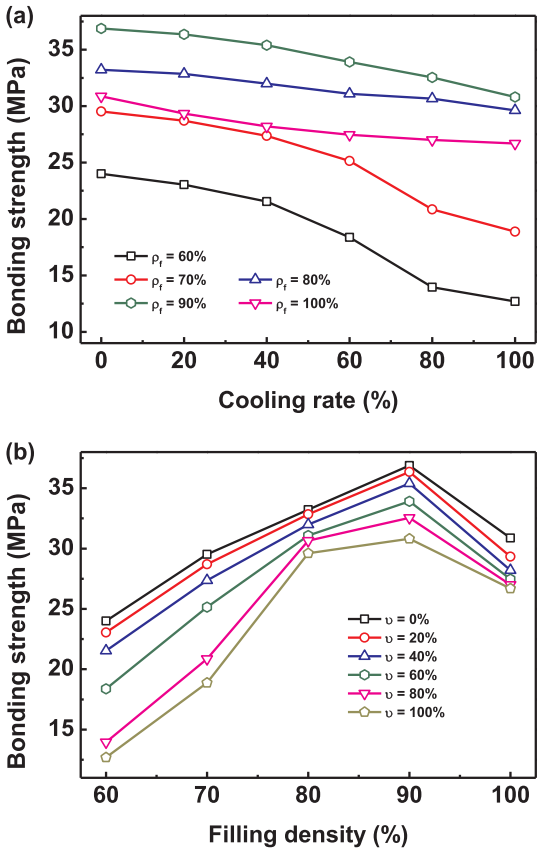

Fig. 1. The effect of (a) cooling rate υ with different filling density ρ_f and (b) filling density ρ_f with different cooling rate υ on the interfacial bonding strength for the FDM 3D-printed samples.

cooling rate decreases from 100% to 80% to 60% to 40% to 20% and then to 0%, respectively. Moreover, at relative lower filling density (ρ_f = 60% and 70%, corresponding to the black and red line in Fig. 1a, respectively), the cooling rate exhibits a dramatic impact on the interfacial bonding strength, where the interfacial bonding strength is improved by about 89% (ρ_f = 60%) and 56% (ρ_f = 70%) as υ decreases from 100% to 0%. However, at relative higher filling density (ρ_f = 80%, 90%, and 100%), the effect of cooling rate on the interfacial bonding strength is weak, where the interfacial bonding strength is just improved by about 12% (ρ_f = 80%), 20% (ρ_f = 90%), and 16% (ρ_f = 100%) as υ decreases from 100% to 0%. That is to say that the interfacial bonding strength can be markedly tailored by the cooling rate when the filling density is relative lower and is less dependent on the cooling rate as long as the filling density is high enough.

The effect of filling density on the interfacial bonding strength at a certain fixed cooling rate, as presented in Fig. 1b, shows an unusual and interesting phenomenon that, as the filling density increases from 60% to 100%, the interfacial bonding strength firstly increases to an optimal value at ρ_f = 90% and then decreases. The decrease in the interfacial bonding strength when ρ_f increases from 90% to 100% indicates that the FDM 3D-printed parts could simultaneously possess high interfacial bonding strength and low weight (or low ρ_f). Note that the lower filling density represents the lighter weight and the less usage of the 3D printing filament because of the higher porosity [10]. Take the cooling rate υ = 100% as an example (the dark yellow line in Fig. 1b), the interfacial bonding strength gradually increases from 12.7 MPa to 18.9 MPa to 29.6 MPa to 30.8 MPa and then decreases to 26.7 MPa as the filling density increases from 60% to 70% to 80% to 90% and then to 100%, respectively. Moreover, at relative lower cooling rate (υ = 0%, 20%, 40%, and 60%), the effect of filling density on the interfacial bonding strength is weaker, where the interfacial bonding strength is improved by about 54% (υ = 0%), 58% (υ = 20%), 64% (υ = 40%), and 85% (υ = 60%) as ρ_f increases from 60% to 90%. However, at relative higher cooling rate (υ = 80% and 100%), the effect of cooling rate on the interfacial bonding strength is much more marked, where the interfacial bonding strength is improved by about 133% (υ = 80%) and 143% (υ = 100%) as ρ_f increases from 60% to 90%. Likewise, it can be concluded that the interfacial bonding strength is less dependent on the filling density when the cooling rate is relative lower and can be markedly tailored by the filling density as long as the cooling rate is higher.

3.2. Elongation at break

In addition to the interfacial bonding strength, the elongation at break is also an important indicator to measure the mechanical quality of the FDM 3D-printed parts and the study on it (Fig. 2) greatly contribute to understanding of the interfacial bonding mechanism. As compared with Fig. 1, the variation trends of the elongation at break (Fig. 2) are completely identical to the interfacial bonding strength (Fig. 1); namely, the stronger interfacial bonding exhibits the larger elongation at break for the FDM 3D-printed parts. It is well known that the mechanical properties of the FDM 3D-printed parts are attributed to the interfacial adhesion between two adjacent extruded layers. Similar to polymer healing process [26–31], the adhesion of two layers of molten polymers during FDM process can be described by two steps: (1) surface contact, followed by (2) inter-molecular diffusion of polymer chain segments across the wetted interfaces [21,32–35]. Thus, the strength of interfacial adhesion is determined by the formation of wetted interface and degree of inter-molecular diffusion between two extruded layers and also the diffusive mechanism of adhesion could be proposed to explain how one extruded layers sticks to another [21,33].

3.3. Fracture-surface morphologies

To study the interfacial adhesion behaviors of the FDM process, we further examined the fracture-surface morphologies of the FDM 3D-printed samples with filling density ρ_f = 100% at different cooling rate υ, as illustrated in Fig. 3. It can be seen that the fractured surfaces become much more smooth as the cooling rate increases, indicating that the weaker interfacial adhesion occurs at higher cooling rate (larger υ). Note that the rougher fracture surfaces mean larger wetted interfaces and degree of inter-molecular diffusion between two adjacent extruded layers, and the formation of them needs to absorb more fracture energy. Therefore, it can prove that the higher cooling rate induces the larger wetted interfaces and degree of inter-molecular diffusion to effectively disperse the stress acting on the interfacial bonding area and absorb more fracture energy, which availably strengthens the interfacial bonding adhesion.

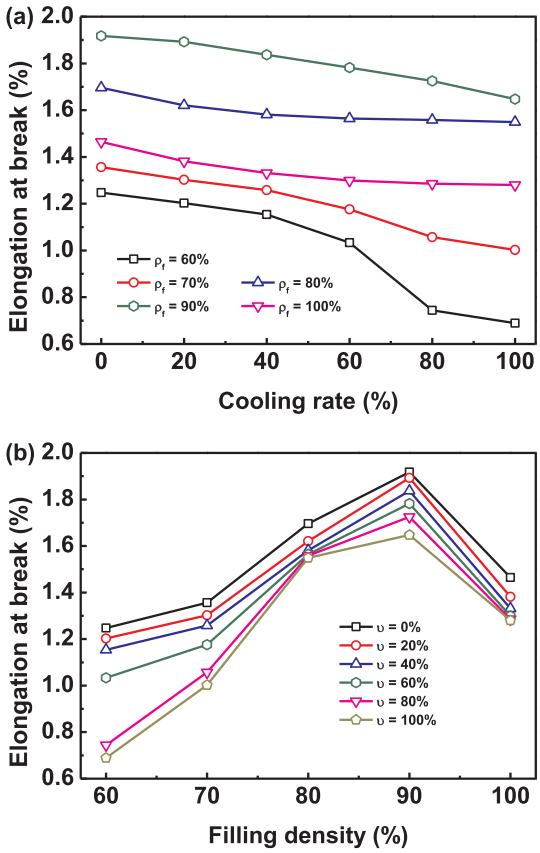

Fig. 2. The effect of (a) cooling rate υ with different filling density ρ_f and (b) filling density ρ_f with different cooling rate υ on the elongation at break for the FDM 3D-printed samples.

3.4. Interfacial width calculated by SCFT

The behavior that the lower cooling rate υ leads to stronger interfacial adhesion can be also rationalized by considering the width of wetted interfaces (interfacial width). Here, we employed the extended self-consistent field theory to examine the interfacial width (we define the width as $w \equiv (\mathrm{d}\phi/\mathrm{d}z)^{-1}$ evaluated at the interface [36]), as presented in Fig. 4. As can be seen, the interfacial width becomes narrower rapidly as $\chi_{AB}N$ increases from 0 to 20, where the other interaction parameters used in the SCFT calculations were fixed at $\chi_{AH}N = \chi_{AW}N = \chi_{BH}N = \chi_{HW}N = 20$ and $\chi_{BW}N = 0$. Moreover, as $\chi_{AB}N$ increases, the interfacial width first narrow rapidly at relatively low $\chi_{AB}N$ and then slightly at relatively high $\chi_{AB}N$. Note that the larger $\chi_{AB}N$ corresponds to the larger cooling rate υ and vice versa, i.e. $\chi_{AB}N \propto \upsilon$. To make a comparison with the experimental results, we have also placed the cooling rate υ in the corresponding location in Fig. 4. Combining with the experimental results (Figs. 2 and 3), they all

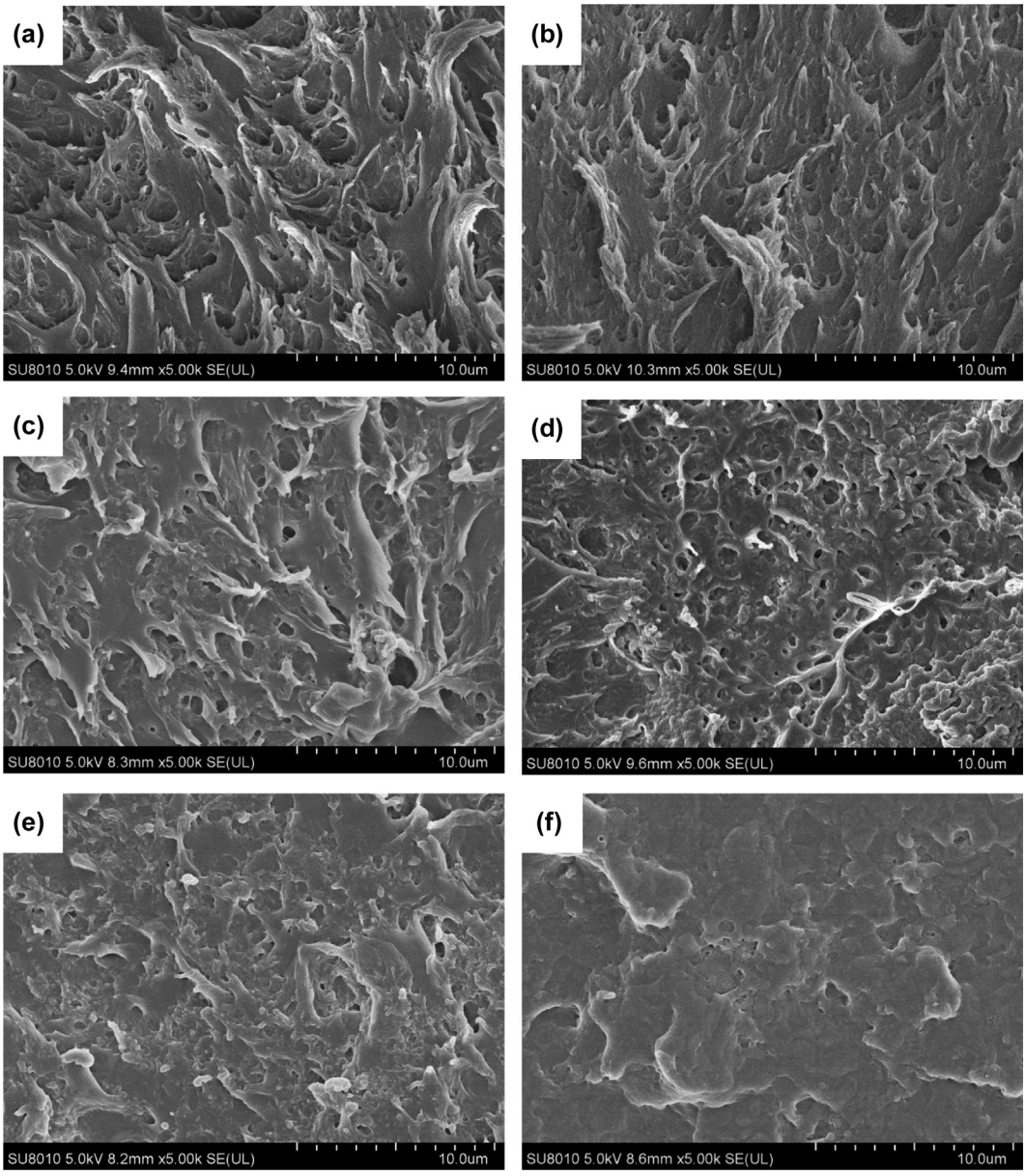

Fig. 3. SEM of the fractured morphologies of the FDM 3D-printed samples with filling density ρ_f = 100% at different cooling rate: (a) υ = 0%, (b) υ = 20%, (c) υ = 40%, (d) υ = 60%, (e) υ = 80%, and (f) υ = 100%.

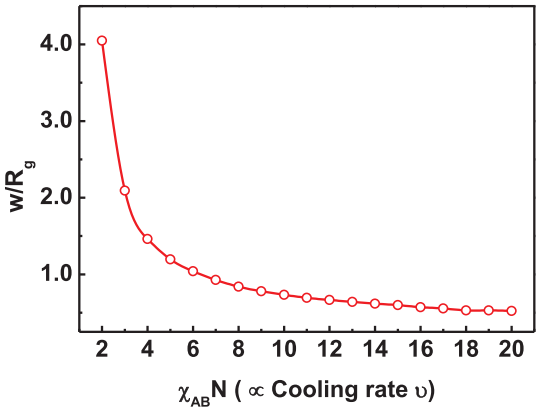

Fig. 4. Interfacial width w/R_g of the interface between currently-extruded (A) and previously-deposited (B) layers calculated by the self-consistent field theory.

elucidate that the lower cooling rate υ (smaller $\chi_{AB}N$) forms broader wetted interfaces (interfacial width) and the larger degree of intermolecular diffusion between two adjacent deposited layers.

4. Conclusions

In summary, the controllable interfacial adhesion behaviors of polymer-on-polymer surfaces during FDM 3D printing process were examined by combining the experimental tests and SCFT calculations. Our results show that the interfacial bonding strength is markedly determined by the filling density ρ_f and cooling rate υ, where the higher filling density ρ_f and lower cooling rate υ would strengthen the interfacial adhesion or bonding, and vice versa. The interfacial bonding strength is less (or more) dependent on the filling density ρ_f (or cooling rate υ) when the cooling rate υ (or filing density ρ_f) is relative lower and can be markedly (or slightly) tailored by the filling density ρ_f (or cooling rate υ) as long as the cooling rate υ (or filling density ρ_f) is higher. Moreover, an unusual and interesting phenomenon was observed that the interfacial bonding strength firstly increases to an

optimal value at $\rho_f = 90\%$ and then decreases as the filling density increases from 60% to 100%. The present results may provide useful information for preparing lightweight FDM parts with high mechanical properties and a general understanding of the interfacial bonding behaviors of polymer-on-polymer surfaces. Beyond this work, it still remains a number of opportunities for further discovery both in fundamental and applied work with different FDM 3D printing parameters as well as different polymers because of the distinct characteristics among them, such as the sensitivity of polymers to temperature, which is worth to be demonstrated to expedite the development of the theory of the interfacial bonding behaviors and the practical applications of FDM 3D printing technologies.

Declaration of Competing Interest

The authors declare that they have no known competing financial interests or personal relationships that could have appeared to influence the work reported in this paper.

Acknowledgements

This work was financially supported by the State's Key Project of Research and Development Plan (Grant No.: 2016YFB1100900), the Regional Key Program of Science and Technology Service Network Initiative from Chinese Academy of Sciences, the Key Research Project of Jiangxi Province (Grant No.: 20192ACB80002), the Fund of National Engineering and Research Center for Commercial Aircraft Manufacturing, the STS Project of Fujian-CAS (Grant No.: 2017T3005, 2019T3013, 2019T3016, and 2019T3018), the Fund of National Engineering Research Center for Optoelectronic Crystalline Materials. Support from CAS Key Laboratory of Design and Assembly of Functional Nanostructures, and Fujian Key Laboratory of Nanomaterials, Fujian Institute of Research on the Structure of Matter, Chinese Academy of Sciences, Fuzhou, Fujian 350002, China (2013DP173231) is also appreciated.

Author contributions

Xu Zhang: Mechanical test, Data processing, Theoretical calculations, Writing-Original draft preparation, reviewing, and editing.

Jianlei Wang: Modification of FDM 3D model, FDM 3D printing process for experimental samples, Filament preparation for FDM 3D printing.

References

[1] J.U. Lind, T.A. Busbee, A.D. Valentine, F.S. Pasqualini, H. Yuan, M. Yadid, S.J. Park, A. Kotikian, A.P. Nesmith, P.H. Campbell, J.J. Vlassak, J.A. Lewis, K.K. Parker, Instrumented cardiac microphysiological devices via multimaterial three-dimensional printing, Nat. Mater. 16 (2017) 303.

[2] C. Minas, D. Carnelli, E. Tervoort, A.R. Studart, 3D printing of emulsions and foams into hierarchical porous ceramics, Adv. Mater. 28 (2016) 9993–9999.

[3] B. Huang, H. He, S. Meng, Y. Jia, Optimizing 3D printing performance of acrylonitrile-butadiene-styrene composites with cellulose nanocrystals/silica nanohybrids, Polym. Int. 68 (7) (2019) 1351–1360.

[4] B. Nasri-Nasrabadi, A. Kaynak, S. Seyedin, Z. Komeily-Nia, A.Z. Kouzani, Nanogrooved carbon microtubes for wet three-dimensional printing of conductive composite structures, Polym. Int. 68 (5) (2019) 922–928.

[5] S. Miao, W. Zhu, N.J. Castro, M. Nowicki, X. Zhou, H. Cui, J.P. Fisher, L.G. Zhang, 4D printing smart biomedical scaffolds with novel soybean oil epoxidized acrylate, Sci. Rep. 6 (2016) 27226.

[6] O.S. Carneiro, A.F. Silva, R. Gomes, Fused deposition modeling with polypropylene, Mater. Des. 83 (2015) 768–776.

[7] E. Balčiūnas, S.J. Baldock, N. Dreižė, M. Grubliauskaitė, S. Coultas, D.L. Rochester, M. Valius, J.G. Hardy, D. Baltriukienė, 3D printing hybrid organometallic polymer-based biomaterials via laser two-photon polymerization, Polym. Int. 68 (11) (2019) 1928–1940.

[8] G.A. Appuhamillage, D.R. Berry, C.E. Benjamin, M.A. Luzuriaga, J.C. Reagan, J.J. Gassensmith, R.A. Smaldone, A biopolymer-based 3D printable hydrogel for toxic metal adsorption from water, Polym. Int. 68 (5) (2019) 964–971.

[9] J. Wang, H. Xie, L. Wang, T. Senthil, R. Wang, Y. Zheng, L. Wu, Anti-gravitational 3D printing of polycaprolactone-bonded Nd-Fe-B based on fused deposition modeling, J. Alloys Compd. 715 (2017) 146–153.

[10] J. Wang, T. Senthil, L. Wu, X. Zhang, Enhancement of lightweight composite parts with robust cellular structures by combining fused deposition modeling and electromagnetic induction heating, Adv. Eng. Mater. 20 (2018) 1800215.

[11] Y. Li, J. Zhong, L. Wu, Z. Weng, L. Zheng, S. Peng, X. Zhang, High performance POSS filled nanocomposites prepared via UV-curing based on 3D stereolithography printing, Compos. Part A: Appl. Sci. Manuf. 117 (2019) 276–286.

[12] Y. Zheng, R. Wang, X. Dong, L. Wu, X. Zhang, High strength conductive polyamide 6 nanocomposites reinforced by prebuilt three-dimensional carbon nanotube networks, ACS Appl. Mater. Interfaces 10 (2018) 28103–28111.

[13] X. Zhang, L. Wu, J. Wang, Distinct mechanical properties of polymer/polymer-grafting-graphene nanocomposites, Macromol. Chem. Phys. 219 (2018) 1800161.

[14] S. Ahn, M. Montero, M. Odell, S. Roundy, P.K. Wright, Anisotropic material properties of fused deposition modeling ABS, Rapid Prototyp. J. 8 (2002) 248–257.

[15] W. Wu, P. Geng, G. Li, D. Zhao, H.B. Zhang, J. Zhao, Influence of layer thickness and raster angle on the mechanical properties of 3D-printed PEEK and a comparative mechanical study between PEEK and ABS, Materials 8 (2015) 5834–5846.

[16] M. Dawoud, I. Taha, S.J. Ebeid, Mechanical behaviour of ABS: an experimental study using FDM and injection moulding techniques, J. Manuf. Process. 21 (2016) 39–45.

[17] B.M. Tymrak, M. Kreiger, J.M. Pearce, Mechanical properties of components fabricated with open-source 3-D printers under realistic environmental conditions, Mater. Des. 58 (2014) 242–246.

[18] J.M. Chacón, M.A. Caminero, E. García-Plaza, P.J. Núñez, Additive manufacturing of PLA structures using fused deposition modelling: effect of process parameters on mechanical properties and their optimal selection, Mater. Des. 124 (2017) 143–157.

[19] I. Durgun, R. Ertan, Experimental investigation of FDM process for improvement of mechanical properties and production cost, Rapid Prototyp. J. 20 (2014) 228–235.

[20] J. Wang, H. Xie, Z. Weng, T. Senthil, L. Wu, A novel approach to improve mechanical properties of parts fabricated by fused deposition modeling, Mater. Des. 105 (2016) 152–159.

[21] J. Yin, C. Lu, J. Fu, Y. Huang, Y. Zheng, Interfacial bonding during multi-material fused deposition modeling (FDM) process due to inter-molecular diffusion, Mater. Des. 150 (2018) 104–112.

[22] S. Gantenbein, K. Masania, W. Woigk, J.P.W. Sesseg, T.A. Tervoort, A.R. Studart, Three-dimensional printing of hierarchical liquid-crystal-polymer structures, Nature 561 (2018) 226–230.

[23] J.U. Kim, M.W. Matsen, Droplets of structured fluid on a flat substrate, Soft Matter 5 (2009) 2889–2895.

[24] A.W. Bosse, C.J. Garcia-Cervera, G.H. Fredrickson, Microdomain ordering in laterally confined block copolymer thin films, Macromolecules 40 (2007) 9570–9581.

[25] X. He, Z. Zou, D. Kan, H. Liang, Self-assembly of diblock copolymer confined in an array-structure space, J. Chem. Phys. 142 (2015) 101912.

[26] J. Wang, Y. Li, L. Zheng, L. Wu, H. Wang, X. Zhang, Self-assembly behaviors of graft copolymer structured fluid droplets on flat solid surfaces, Chem. Phys. Lett. 721 (2019) 43–48.

[27] J. Lin, S. Gong, X. Zhang, L. Wang, Hierarchical microstructures self-assembled from linear multiblock copolymers in thin films, Macromol. Theory Simul. 24 (2015) 468–476.

[28] J. Wang, Y. Li, L. Zheng, H. Wang, L. Wu, X. Zhang, Morphology transformation of micelles self-assembled from amphiphilic coil-coil diblock copolymer/nanoparticle mixture in dilute solution by combining self-consistent field theory and density functional theory, Chem. Phys. Lett. 710 (2018) 215–220.

[29] R.P. Wool, K.M. O'Connor, A theory of crack healing in polymers, J. Appl. Phys. 52 (1981) 5953–5963.

[30] M. Zhu, M.Z. Rong, M.Q. Zhang, Self-healing polymeric materials towards non-structural recovery of functional properties, Polym. Int. 63 (10) (2014) 1741–1749.

[31] S. Xu, D. Sheng, X. Liu, F. Ji, Y. Zhou, L. Dong, H. Wu, Y. Yang, A seawater-assisted self-healing metal-catechol polyurethane with tunable mechanical properties, Polym. Int. 68 (6) (2019) 1084–1090.

[32] R.P. Wool, B.-L. Yuan, O.J. McGarel, Welding of polymer interfaces, Polym. Eng. Sci. 29 (1989) 1340–1367.

[33] N. Maeda, N. Chen, M. Tirrell, J.N. Israelachvili, Adhesion and friction mechanisms of polymer-on-polymer surfaces, Science 297 (2002) 379–382.

[34] N. Roy, E. Buhler, J.-M. Lehn, Double dynamic self-healing polymers: supramolecular and covalent dynamic polymers based on the bis-iminocarbohydrazide motif, Polym. Int. 63 (8) (2014) 1400–1405.

[35] I. Kammakakam, K.E. O'Harra, G.P. Dennis, E.M. Jackson, J.E. Bara, Self-healing imidazolium-based ionene-polyamide membranes: an experimental study on physical and gas transport properties, Polym. Int. 68 (6) (2019) 1123–1129.

[36] M.W. Matsen, F.S. Bates, Unifying weak- and strong-segregation block copolymer theories, Macromolecules 29 (1996) 1091–1098.